Journal of Biomechanics 42 (2009) 1705–1712

Contents lists available at ScienceDirect

Journal of Biomechanics

journal homepage: www.elsevier.com/locate/jbiomech
www.JBiomech.com

Validation of a fluid–structure interaction numerical model for predicting flow transients in arteries

V. Kanyanta *, A. Ivankovic, A. Karac

School of Electrical, Electronics and Mechanical Engineering, University College Dublin, Ireland

ARTICLE INFO

Article history:
Accepted 15 April 2009

Keywords:
Fluid–structure interaction
Numerical model validation
Blood flow

ABSTRACT

Fluid–structure interaction (FSI) numerical models are now widely used in predicting blood flow transients. This is because of the importance of the interaction between the flowing blood and the deforming arterial wall to blood flow behaviour. Unfortunately, most of these FSI models lack rigorous validation and, thus, cannot guarantee the accuracy of their predictions. This paper presents the comprehensive validation of a two-way coupled FSI numerical model, developed to predict flow transients in compliant conduits such as arteries. The model is validated using analytical solutions and experiments conducted on polyurethane mock artery. Flow parameters such as pressure and axial stress (and precursor) wave speeds, wall deformations and oscillating frequency, fluid velocity and Poisson coupling effects, were used as the basis of this validation. Results show very good comparison between numerical predictions, analytical solutions and experimental data. The agreement between the three approaches is generally over 95%. The model also shows accurate prediction of Poisson coupling effects in unsteady flows through flexible pipes, which up to this stage have only being predicted analytically. Therefore, this numerical model can accurately predict flow transients in compliant vessels such as arteries.

1. Introduction

Fluid–structure interaction (FSI) problems are of significant importance and, with respect to modelling issues, are also very challenging multi-physics problems. One example where FSI plays an important role is in biomedical flow involving compliant blood vessels (Yang et al., 2007; Bluestein et al., 2008; Kock et al., 2008), heart valve (Nobili et al., 2008) and human airways (Kittisak and Ramana, 2008).

Blood flow through a compliant artery requires appropriate fluid–structure coupling in order to account for the interaction between the flowing blood and the deforming arterial wall. Earlier numerical models used to predict blood flow were based on rigid, idealised (Steinman et al., 2000; Bertolotti et al., 2000) or patient specific (Steinman et al., 2002; Myers et al., 2001), arterial geometries, where this interaction was not taken into account. Although much attention was given to the complex flow patterns in arteries, the deformation of the arterial wall during each contraction and expansion of the heart was ignored. In an attempt to resolve this, some studies used time-varying geometries such as the work of Zeng et al. (2003) and Pivkin et al. (2004). Many recent studies now employ FSI approach to predict blood flow in arteries (Yang et al., 2007; Bluestein et al., 2008; Kock et al., 2008; Scotti et al., 2008). However, many of these FSI models lack rigorous validation and, thus, cannot guarantee the accuracy of their predictions.

This paper presents the validation of a FSI model developed to predict flow transients in flexible conduits such as arteries (Greenshields et al., 1999; Karac and Ivankovic, 2003). The model was validated using analytical solutions and experiments conducted on a straight polyurethane mock artery of inner diameter $d = 10$ mm, thickness $b = 0.5$ mm and length $l = 900$ mm. Flow transients such as pressure, axial stress and precursor wave speeds, mock artery deformations and oscillating frequency and fluid velocity and Poisson coupling effects were used as the basis of this validation. Numerical simulations are performed using OpenFOAM, a 3D finite volume method C++ library (Wikki Ltd., www.wikki.co.uk). The mechanical properties of the mock artery were based on measured values (Kanyanta and Ivankovic, 2009).

2. Experimental and numerical methods

The experimental set-up was as shown in Fig. 1. The inflow tank is used to provide a pressure head and the solenoid valves (V1 and V2) control the flow through the mock artery. Pulsatile/unsteady flow conditions are achieved by the opening and closing of V1 or V2, which is controlled according to the user-defined control function, taking the form of the desired pressure waveform (Kanyanta, 2009). The typical pressure waveforms obtained by this method are shown in

* Corresponding author. Tel.: +353 1 716 1880.
E-mail address: valentine.kanyanta@ucd.ie (V. Kanyanta).

0021-9290/$ - see front matter © 2009 Elsevier Ltd. All rights reserved.
doi:10.1016/j.jbiomech.2009.04.023

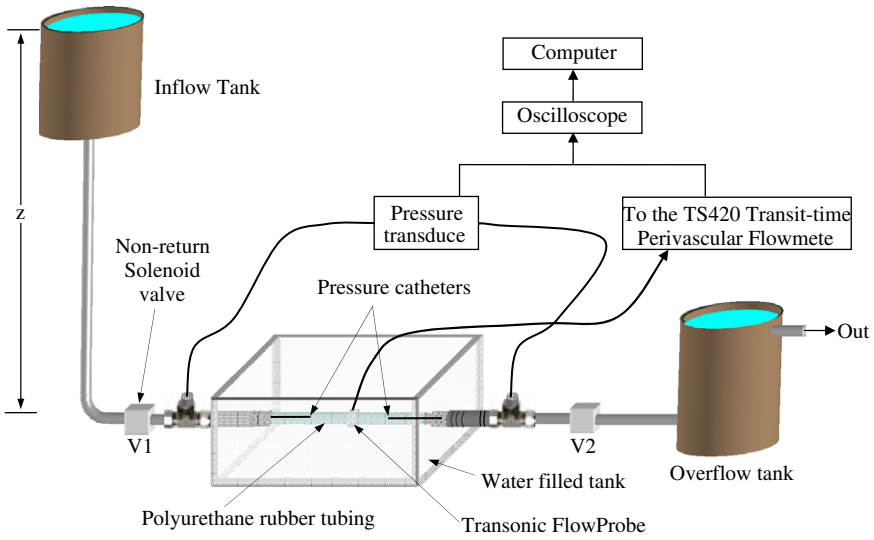

Fig. 1. Schematic of the experiment set-up for flow transients in a straight water-filled polyurethane mock artery.

Fig. 2. Pressure and flow rates were measured using pressure transducers and a TS420 transit-time Perivascular Flowmeter, respectively. Three methods were used in determining pressure wave speed in the mock artery; foot-to-foot, differential pressure and pressure–velocity (PU) loop method.

Foot-to-foot method involves measurement of either pressure or velocity waveforms at two sites, which are a known distance Δx apart along the length of the mock artery. In this case, pressure wave speed C_f is given by

$$C_f = \frac{\Delta x}{\Delta t}, \tag{1}$$

where Δt is the time taken for the wave to travel from one measuring site to the other.

In the differential pressure method, differential pressure between two sites, along the length of the mock artery, and flow rate midway between the two sites, are measured simultaneously. The pressure wave speed is then given by

$$C_f = \frac{\Delta P_{\max}}{\rho_f V_{\max}}, \tag{2}$$

where $\Delta P_{\max}$ is the maximum differential pressure, $V_{\max}$ is the maximum flow velocity and ρ_f is the fluid density.

The theoretical basis of the PU-loop method is the water hammer equation, which for backward and forward travelling waves can be expressed as (Khir et al., 2007)

$$dP_{\pm} = \pm \rho_f C_f V_{\pm}. \tag{3}$$

Pressure and velocity (flow rate) are simultaneously measured at a given site along the length of the mock artery. Plotting pressure and velocity over a cycle gives the PU-loop. During the early part of the cycle where only forward travelling waves are hypothesised to be present, the slope of the PU-loop should be linear, and can be given by $S_0 = dP_+/dV_+ = \rho C_f$.

Fluid velocity was determined from the measured flow rate Q, assuming a velocity profile given by Eq. (4), with $n = 7$. This profile was arrived at after comparing experimental and simulated flow waveforms for different velocity profiles (Kanyanta, 2009). Although the flow in this case is laminar, there is insufficient time for a parabolic velocity profile to develop during each cycle, as can be shown by the Wormesley's number $\alpha = 13.7$ (Eq. (5)). Pressure perturbations were derived from the measured pressure waveforms. Axial stress wave speed and mock artery oscillating frequency could not be determined experimentally due to the current experimental limitations.

$$V_{\max} = \frac{Q(n+1)(2n+1)}{n^2 2\pi R^2}, \tag{4}$$

$$\alpha = r\sqrt{\frac{\rho_f \omega}{\eta}}, \quad \omega = 7.54\,\text{rad/s}, \quad \eta = 0.001\,\text{Ns/m}^2. \tag{5}$$

Numerical studies were performed using a two-way FSI coupling scheme (Fig. 3) implemented in OpenFOAM (Greenshields et al., 1999; Karac and Ivankovic, 2003). Here, the fluid and solid parts of the solution domain form separate meshes, but the interface boundary shares the same location in space. The solid and fluid models are combined within a single code and information exchange, in terms of tractions and displacements, takes place at the fluid–solid interface.

Since deformations are small, the solid domain was modelled as a linear elastic solid, using the properties of polyurethane elastomer under wet-room temperature (Kanyanta and Ivankovic, 2009) i.e. Young's modulus, $E = 5.3$ MPa, density, $\rho = 1000\,\text{kg/m}^2$ and Poisson ratio, $\nu = 0.4995$. The fluid domain was modelled as a compressible Newtonian fluid with dynamic viscosity $\eta = 0.001\,\text{Ns/m}^2$, density $\rho_f = 998\,\text{kg/m}^3$ and bulk modulus $K = 2.2$ GPa (corresponding to the properties of water at 20 °C).

3. Mathematical formulation

The behaviour of a continuum in Eulerian frame reference is governed by the following equations:

- Mass balance, or continuity equation

$$\frac{\partial \rho}{\partial t} + \nabla \cdot (\rho \mathbf{V}) = 0 \tag{6}$$

- Momentum balance, or Cauchy's first law of motion (neglecting body forces)

$$\frac{\partial \rho \mathbf{V}}{\partial t} + \nabla \cdot (\rho \mathbf{V}\mathbf{V}) = \nabla \cdot \boldsymbol{\sigma}, \tag{7}$$

where ρ is the density, $\mathbf{V}$ is the velocity and $\boldsymbol{\sigma}$ is the stress tensor. The constitutive laws for a linear elastic (Hookean) solid and Newtonian fluid are

- Stress–strain relation for a Hookean solid

$$\boldsymbol{\sigma} = 2\mu\boldsymbol{\varepsilon} + \lambda \text{tr}(\boldsymbol{\varepsilon})\mathbf{I} \tag{8}$$

- Stress–strain rate relation for a Newtonian fluid (Stokes's law)

$$\boldsymbol{\sigma} = 2\eta\dot{\boldsymbol{\varepsilon}} - \frac{2}{3}\eta \text{tr}(\dot{\boldsymbol{\varepsilon}})\mathbf{I} - p\mathbf{I}, \tag{9}$$

where μ and λ are Lame' coefficients, $\boldsymbol{\varepsilon} = 1/2[\nabla\mathbf{U} + (\nabla\mathbf{U})^T]$ is the strain tensor, $\mathbf{U}$ is the displacement vector, $\mathbf{I}$ is the identity tensor, η is the dynamic viscosity, $\dot{\boldsymbol{\varepsilon}} = 1/2[\nabla\mathbf{V} + (\nabla\mathbf{V})^T]$ is the deformation rate and p is the hydrostatic pressure.

In the case of a linear elastic solid, the continuity equation need not to be considered and since the deformations are sufficiently small, the convection term $\nabla \cdot (\rho\mathbf{V}\mathbf{V})$ can be neglected and $\mathbf{V}$ becomes $\partial\mathbf{U}/\partial t$, and the analysis in the Eulerian and Lagrange formulations are almost identical. A single equation can then be derived for the structure (solid domain) in terms of $\mathbf{U}$ as in Eq. (10)

$$\frac{\partial}{\partial t}\left(\rho \frac{\partial \mathbf{U}}{\partial t}\right) = \nabla \cdot [\mu\nabla\mathbf{U} + \mu(\nabla\mathbf{U})^T + \lambda\mathbf{I}\text{tr}(\nabla\mathbf{U})]. \tag{10}$$

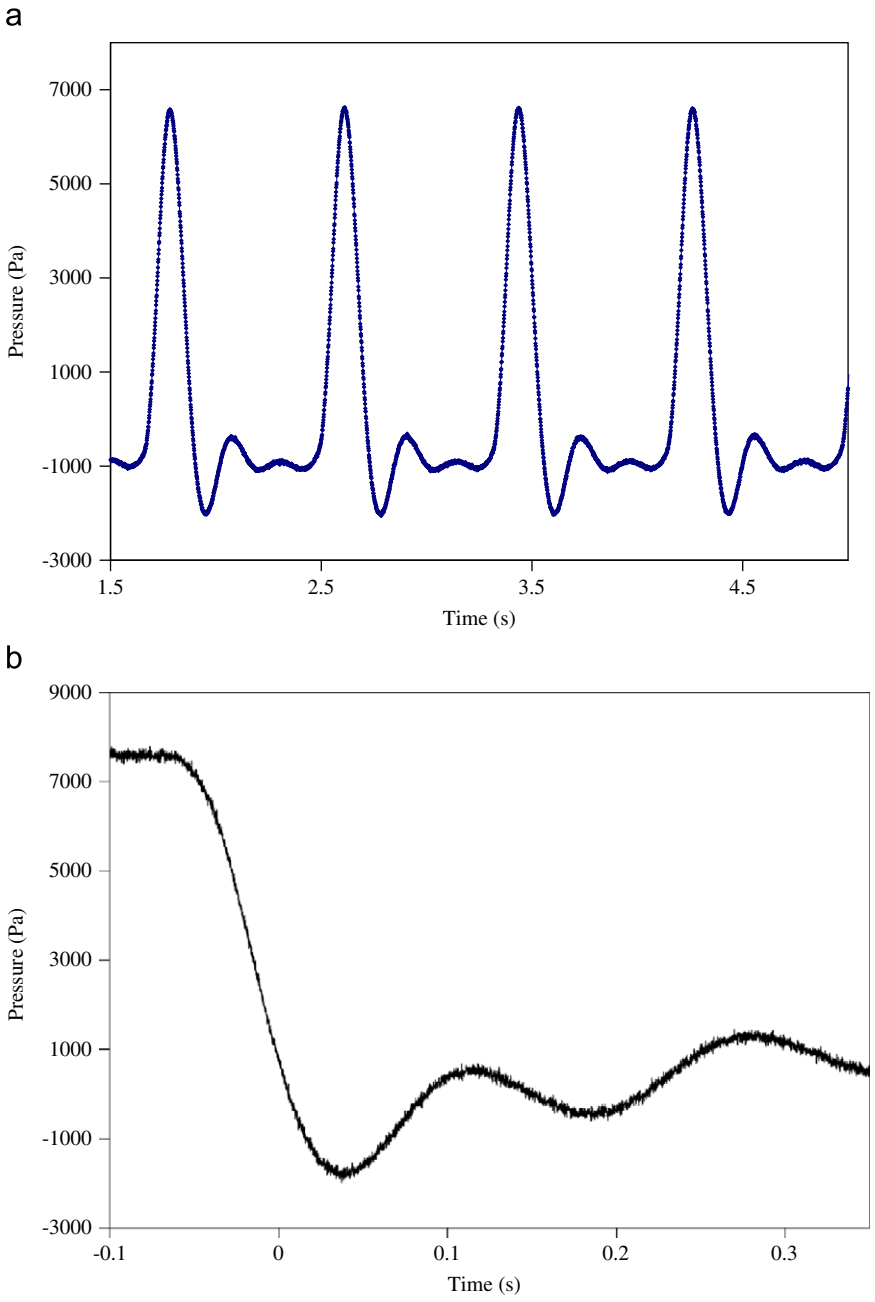

Fig. 2. Typical pressure waveform(s) generated experimentally: (a) pulsatile and (b) sudden valve (V2) opening.

For the fluid flow, both the continuity equation and the momentum balance must be satisfied and the convection term cannot be ignored. The momentum balance, in terms of velocity **V**, hence becomes

$$\frac{\partial(\rho\mathbf{V})}{\partial t} + \nabla\cdot(\rho\mathbf{V}\mathbf{V}) = \nabla\cdot\eta\left[\nabla\mathbf{V} + (\nabla\mathbf{V})^T - \frac{2}{3}\mathbf{I}\mathrm{tr}(\nabla\mathbf{V})\right] - \nabla p. \quad (11)$$

The system of fluid equations is closed by relating pressure and density of compressible liquids by bulk modulus K

$$K = \rho\frac{\partial p}{\partial \rho}. \quad (12)$$

For small values of ρ/ρ_0 (low pressures), Eq. (12) can be expressed via the well-known barotropic equation

$$\rho = \rho_0 + \psi(p - p_0), \text{ where } \psi = \frac{\rho_0}{K}, \quad (13)$$

and the subscript 0 represents reference values. The pressure implicit with splitting of operators (PISO) algorithm is used to solve the discretised pressure–velocity coupled equations.

Since FVM is based on numerical integration of the system of equations over a computational domain, the time domain is discretised into a finite number of time steps and the spatial domain subdivided into a finite number of contiguous control volumes or cells. Dependent variables and material properties are stored at cell centroids. Numerical integration employs the mid-point rule and linear interpolation of the dependent variables between the cell centroids is assumed.

4. Numerical model validation

The numerical model was validated by comparing its predictions of flow transients in a straight water-filled polyurethane

mock artery to analytical solutions and experimental data. The problem description is shown in Fig. 4. The problem is axi-symmetric and therefore only required a solution domain in 2D. Different mesh densities were tested until a converged solution that is independent of mesh density (or size) was obtained (i.e. 800 cells along the pipe length, 40 cells across the fluid domain and 3 cells across the solid domain). Wave propagation was initiated at the left end of the pipe by applying a fixed step change in pressure of $p = 7.5$ kPa. Each analysis was run using a time step to ensure Courant number <1. The left pipe wall boundary was treated as a plane of symmetry and the outer wall had zero traction boundary condition (Fig. 4). The fluid inlet boundary was fixed pressure and zero velocity gradient while a convective outflow boundary (Hasan et al., 2005) was applied at the fluid outlet and right pipe wall boundary. Structure displacements were solved using the incomplete-Cholesky conjugate gradient (ICCG) method to a tolerance of 10^{-8}. The incomplete-Cholesky biconjugate gradient (BICCG) method was used for fluid velocity **V** and pressure p due to the asymmetric nature of the coefficient matrix of the system of discretised equations. **V** and p were solved to tolerances of 10^{-5} and 10^{-6}, respectively.

START TIME STEP LOOP ← converge

Solve fluid
- Momentum equation (**V**)
- Pressure (p)
- Velocity correction (**V**) ↺ PISO

Solve structure
- Transfer wall fluid traction to structure
- Momentum equation (**U**) ↺ converge

If fluid boundary is movable (moving mesh)
{
- Displace the fluid mesh boundary with structure boundary displacement **U**
- Recalculate volumes and surface areas for new fluid mesh
- Equate fluid boundary velocity (**V**) to structure boundary velocity ($\partial U/\partial t$)

}
else
{
- Equate fluid boundary velocity (**V**) to structure boundary velocity ($\partial U/\partial t$)

}

END OF TIME STEP

Fig. 3. Implicit solution scheme for fluid–structure interaction (Greenshields et al., 1999).

4.1. Analytical solutions

In a straight unconstrained section of a pipe, the analytical solution of pressure wave speed C_f is given by (Wylie and Streeter, 1993)

$$C_f = \sqrt{\frac{K}{\rho_f}\left[1 + \left(\frac{(d+2b)^2}{b(d+b)} - 2(1-\nu)\right)\frac{K}{E}\right]^{-1}}. \quad (14)$$

Propagating pressure waves are due to both the compressibility of the fluid and the compliance of the structure (pipe). When K is far greater than E, Eq. (14) reduces to

$$C_f^* = \sqrt{\frac{E}{\rho_f}\left(\frac{(d+2b)^2}{b(d+b)} - 2(1-\nu)\right)^{-1}}. \quad (15)$$

In this case, the pressure wave speed is solely due to the stiffness of the pipe. This is generally the case for health arteries. However, this may not be the case for diseased arteries where E can be ten times higher than in health arteries (Ivankovic et al., 2002). Fig. 5 shows the variation of C_f/C_f^* with fluid compressibility for $E = 5.3$ MPa. It is clear that C_f and C_f^* differ significantly for $K<K_s$, solid bulk modulus ($K_s = E/[3(1-2\nu)] = 1.77$ GPa). Therefore, fluid incompressibility assumption can only be used if the bulk modulus of the fluid is equal to or higher than that of the structure (pipe). For the current study, both compressible and incompressible fluid models yielded similar results (Appendix 1).

Eq. (14) only accounts for the change in pipe area, and assumes axial stress to be fixed over the entire pipe length. This results in an overestimation in C_f. A better solution is obtained by applying a

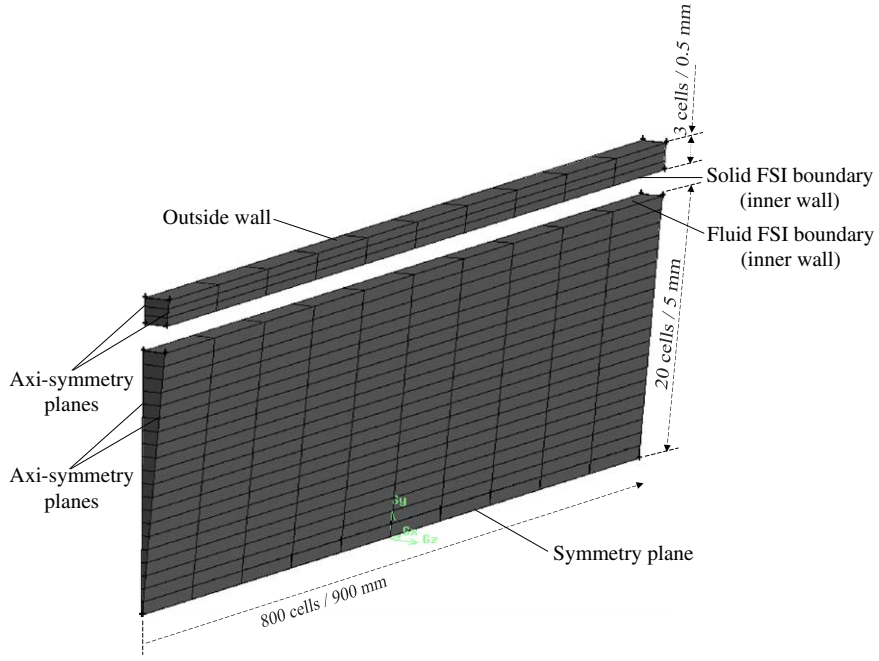

Fig. 4. Axi-symmetry solution domain.

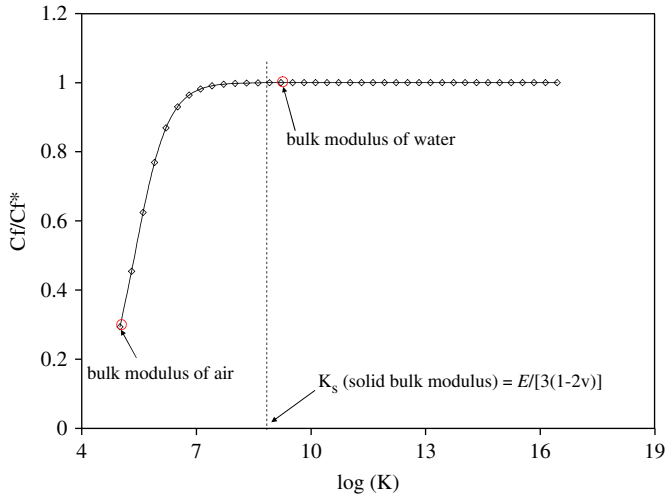

Fig. 5. Variations of C_f/C^*_f with fluid bulk modulus.

factor φ that accounts for the axial stress waves in the pipe wall

$$\varphi = \sqrt{1 - v^2\left[1 + \frac{E}{K}\left(\frac{b}{d}\right)\left(1 - \frac{K\rho_f}{E\rho_s}\right)\right]^{-1}}. \quad (16)$$

The corrected analytical solution for pressure wave speed then becomes

$$\tilde{C}_f = \varphi C_f. \quad (17)$$

The stress wave (precursor wave) speed for an infinitely long plate is given by

$$C_s = \sqrt{\frac{E}{\rho_s}}, \quad (18)$$

and for a thin plate by

$$\tilde{C}_s = \sqrt{\frac{E}{\rho_s(1 - v^2)}}. \quad (19)$$

The relationship between pressure and velocity under unsteady, unidirectional flow is governed by the water hammer equation

$$V_x = \frac{\Delta p}{\rho_f C_f}, \quad (20)$$

where Δp is the pressure difference across the wavefront and V_x is the axial flow velocity.

Three coupling mechanisms exist in FSI: Poisson coupling, friction coupling and junction coupling. Poisson coupling is associated with hoop stress perturbations produced by fluid pressure transients that results in axial stress perturbations through Poisson ratio coefficient. Friction coupling is created by shear stress transients acting on the pipe wall and junction coupling results from the reactions of unbalanced pressure forces and changes in liquid momentum at specific points along the pipe such as bends, tees, valves, etc. Only Poisson coupling effects are discussed in this paper since the work involves flow transients in a straight pipe and friction coupling effects are assumed negligible.

The relationships between axial stress perturbations ($\Delta\boldsymbol{\sigma}$) caused by pressure transients and vice-versa, are given by (Wiggert and Tijsseling, 2001; Tijsseling et al., 2006)

$$\Delta\boldsymbol{\sigma} = -G_s\Delta p \text{ and } \Delta p = -G_f\Delta\boldsymbol{\sigma}, \quad (21)$$

where G_f and G_s are the fluid and solid coupling factors, respectively, given by

$$G_f = -2v\frac{\rho_f}{\rho_s}\left[\left(\frac{C_s}{\tilde{C}_f}\right)^2 - 1\right]^{-1} \text{ and } G_s = 2v\frac{R}{b}\left[\left(\frac{\tilde{C}_s}{C_f}\right)^2 - 1\right]^{-1}, \quad (22)$$

and R is the pipe radius. $\tilde{C}_f$ and $\tilde{C}_s$ are the modified pressure and axial stress wave speeds, given by Eqs. (17) and (19), respectively.

Eq. (21) shows the importance of FSI. Flow transients also include the pipe's natural oscillating frequency, which is discussed under Section 5.1.1.

5. Results

5.1. Numerical model validation

5.1.1. Pressure wave speed, deformations and oscillating frequency

Numerical model predicts pressure wave propagation along the mock artery as presented in Fig. 6(a). Fig. 6(b–d) shows the experimentally determined pressure wave speed using the foot-to-foot, differential pressure and PU-loop methods, respectively. The analytical solution of C_f is determined by Eq. (17), and is equal to 13.31 m/s, while the average experimental value is 13.14 m/s. The simulated value (Fig. 6(a)) is 13.25 m/s, which is 0.4% lower and 0.8% higher than the analytical solution and experimental value, respectively. Fig. 7 shows the comparison between the simulated and analytical solutions of C_f over a wide range of E values.

The other important feature of wave propagation is radial wall deformation shown in Fig. 8(a), with radial displacement of 0.076 mm, which is close to the analytical value approximated by $(d+b)^2p/4Eb = 0.078$ mm. The results also show noticeable oscillations in the wall deformations ahead of the wavefront (Fig. 8(a)). The averaged simulated wavelength for the first oscillation, for $t = 4.8$ ms, is ≈ 0.073 m. Using Eq. (19), the estimated natural frequency becomes 1084 Hz. The analytical solution for the pipe's natural frequency is given by (Tijsseling et al., 2006)

$$f = \frac{1}{2\pi r}\sqrt{\frac{4E}{\rho_s + \alpha(R/b)\rho_f}}. \quad (23)$$

The coefficient α determines the added fluid mass M_f and is given by (Tijsseling et al., 2006)

$$\alpha = \begin{cases} \frac{1}{2} & \text{for } M_f, \text{ ``}A\text{''} = \text{the total mass of the fluid} \\ \frac{1}{3} & \text{for } M_f, \text{ ``}B\text{''} = \frac{2}{3}\text{of the total mass of the fluid} \\ \frac{1}{4} & \text{for } M_f, \text{ ``}C\text{''} = \frac{1}{2}\text{of the total mass of the fluid} \end{cases}. \quad (24)$$

Therefore, the analytical solutions for the frequency are 947 1112, and 1237 Hz for $M_f = A$, B and C respectively. Compared to the simulated frequency, these values are, respectively, 17%, 2% lower and 9% higher. The values obtained with $M_f = B$ and $M_f = C$ are closer to the numerical value than for $M_f = A$. This indicates that only a fraction of the total mass of the fluid contributes to radial deformation. Alternative solutions B and C are based on a linear distribution of radial flow velocity and the validity of this assumption is confirmed by the simulation results presented in Fig. 9(b).

The frequency decreases as the wavefront advances and the deformation of the pipe approach steady state (Fig. 8(b)). The analytical solution is for the instant when the local deformation in the pipe is maximum (i.e. $t = 4.8$ ms), assuming no pipe end effects.

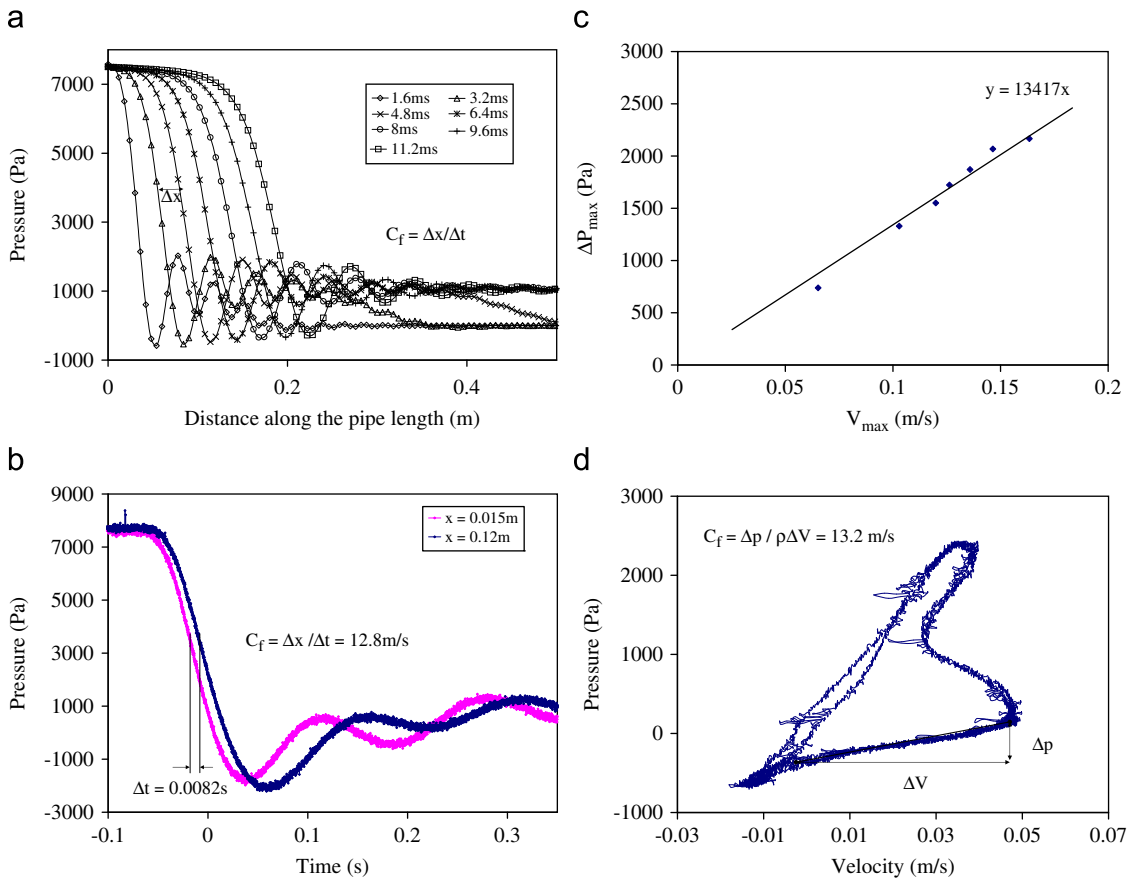

Fig. 6. Pressure wave speed determination using (a) numerical method, (b) experimental foot-to-foot, (c) differential pressure and (d) PU-loop methods.

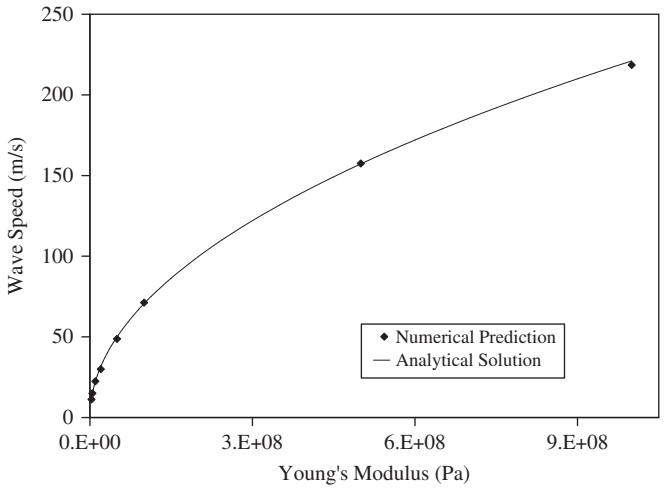

Fig. 7. Predicted pressure wave speed with increasing pipe stiffness.

5.1.2. Fluid particle velocity

Fig. 9(a) presents numerical and analytical predictions of fluid particle flow speed V_x along the pipe centreline, showing good comparison between the two approaches over the entire length of the pipe. The experimental value of V_x was 0.46 m/s, which is about 8% lower than the analytical and simulated values of approximately 0.5 m/s.

5.1.3. Poisson coupling effects

Stress waves in the pipe wall (Fig. 10(b)) are caused by the sudden changes in fluid pressure (Fig. 6(a)). These waves in turn produce pressure perturbations Δp, also known as precursor waves, as shown in Fig. 10(a). Similarly, pressure transients (Fig. 10(a)) produce axial stress perturbations $\Delta\sigma$ shown in Fig. 10(b). The magnitude of Δp and $\Delta\sigma$ is about 14.3% and 13.4% of the primary pressure waves (Fig. 10(a)) and axial stress waves (Fig. 10(b)), respectively. Numerical and analytical values of Δp are 1070 and 1050 Pa, and for $\Delta\sigma$ are −2350 and −2250 Pa, respectively. The experimentally determined magnitude of Δp, corresponding to a change in pressure of 7.5 kPa, is 1200 Pa (Kanyanta, 2009), making the numerical value of Δp 2% higher and 12% lower than the analytical solution and experimental value, respectively, and that of $\Delta\sigma$ 4% higher than its analytical solution. The numerical value of the axial stress wave speed (Fig. 10(b) i.e. $C_s = \Delta x/\Delta t$) is 86.25 m/s and its analytical solution is 84 m/s.

6. Discussion and conclusion

In order to accurately predict blood flow transients, FSI models employed need to be adequately validated. In the current work, experimental data and analytical solutions were employed in order to validate the FSI model for accurate prediction of flow in flexible conduits such as arteries. The results show very good comparison between numerical prediction, analytical solutions and experimental data. The agreement between the three approaches is over 95%, except for the pressure perturbations and axial fluid velocity whose experimental values are 12% higher and 8% lower than the numerical values, respectively. This is thought to be largely due to experimental error. Poisson coupling effects are seen to be an essential and significant component of the flow transient behaviour. Pressure and axial stress perturbations are close to 15% of their respective primary waves.

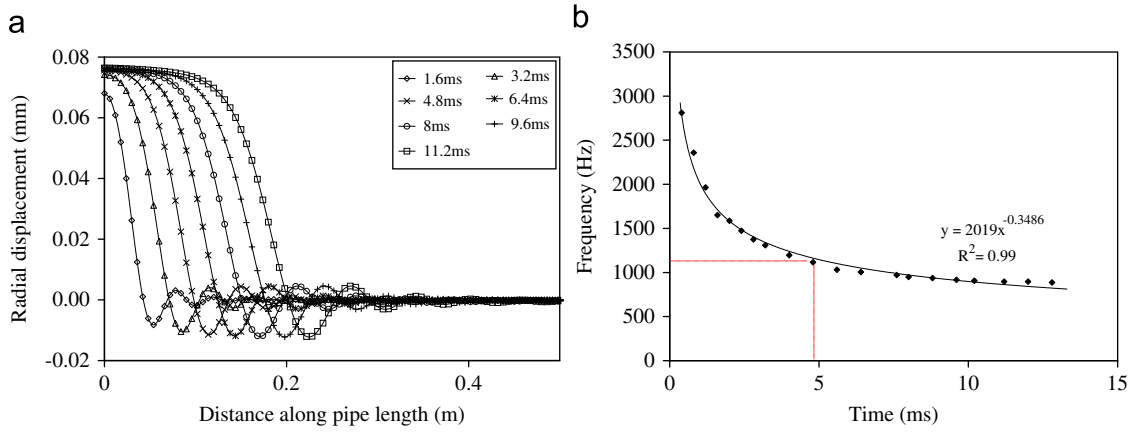

Fig. 8. (a) Radial wall displacement at different time intervals (taken from the mid-wall section) and (b) wall oscillating frequency.

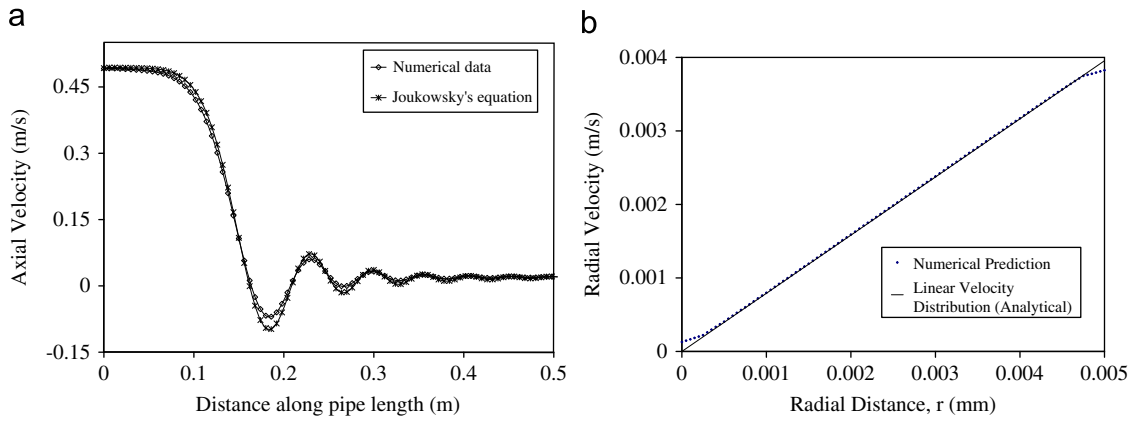

Fig. 9. Comparison between numerical and analytical prediction of (a) axial flow velocity along the mock artery centerline and (b) radial component of fluid velocity field at 80 mm from the mock artery inlet.

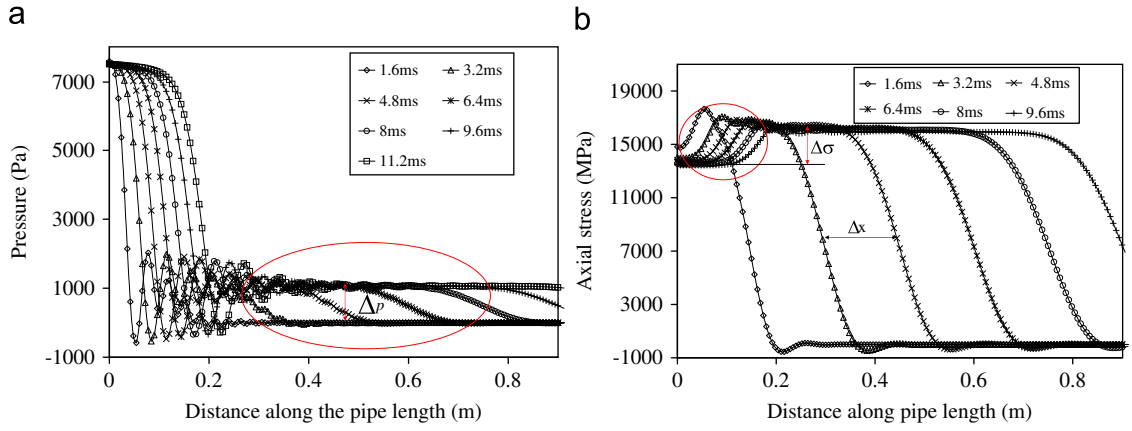

Fig. 10. (a) Pressure perturbations caused by axial stress transients and (b) axial stress perturbations caused by pressure transients.

Since the velocity profile could not be determined experimentally due to the inability to use particle imaging velocimetry technique on a non-transparent mock artery, it was assumed based on the comparison between the measured and simulated flow waveforms (flow rates) for different velocity profiles.

Water and blood are usually modelled as incompressible fluids for simplicity. However, when the bulk modulus of the structure (e.g. arterial wall) is comparable to or greater than the fluid (water or blood) bulk modulus, incompressibility assumption cannot be used in predicting pressure wave speed (Fig. 5). An example would be in diseased arteries (Ivankovic et al., 2002) where artery bulk modulus can be comparable blood bulk modulus. For the current study incompressibility assumption yielded approximately identical results to the compressible fluid model (Appendix 1). However, this is not the case in general and thus, fluid compressibility is preferred in the current model as this would be valid under all possible combinations of K_s and K_f.

The analytical solutions used in this analysis are for an infinitely long pipe with no wave reflections from the pipe ends. This does not affect the comparison of the analytical solutions

with the simulated and experimental data. Flow transients in the mock artery were measured at 0.3 m from the inlet side, which is sufficient to minimise the effect of the constrained (cramped) ends. In the numerical model, a convective outlet boundary is applied at the pipe outlet side, for both the fluid and solid domain in order to avoid the reflection of the axial stress and precursor waves from the pipe outlet. These waves naturally dissipate in the experimental model due to the free outflow surface.

The comparison between the numerical predictions, experimental data and analytical solutions shows that this numerical model can accurately predict flow transients in compliant vessels such as arteries. However, since additional flow features such as flow recirculation, present in flow through branched arterial networks are absent in straight compliant vessels, it may be necessary to validate the model for flow through branched pipes. Future work will clarify this.

Conflict of interest statement

This work is supported by Science Foundation Ireland and all the work presented was conducted at University College Dublin

Acknowledgements

www.wikki.co.uk.
Dr. Neal Murphy, University College Dublin, Ireland.
This work is supported by the Science Foundation Ireland.

Appendix 1. Supporting Information

Supplementary data associated with this article can be found in the online version at doi:10.1016/j.jbiomech.2009.04.023.

References

Bertolotti, C., Deplano, V., 2000. Three-dimensional numerical simulations of flow through a stenosed coronary bypass. Journal of Biomechanics 33, 1011–1022.
Bluestein, D., Alemu, Y., Avrahami, I., Gharib, M., Dumont, K., Ricotta, J.J., Einav, S., 2008. Influence of microcalcifications on vulnerable plaque mechanics using FSI modeling. Journal of Biomechanics 41 (5), 1111–1118.
Greenshields, C.J., Weller, H.G., Ivankovic, A., 1999. The finite volume method for coupled fluid flow and stress analysis. Computational Modelling and Simulation in Engineering 4, 213–218.
Hasan, N., Anwer, S.F., Sanghi, S., 2005. On the outflow boundary condition for external incompressible flows: a new approach. Journal of Computational Physics 206, 661–683.
Ivankovic, A., Karac, A., Dendrinos, E., Parker, K., 2002. Towards early diagnosis of atherosclerosis: the finite volume method for fluid-structure interaction. Biorheology 39, 401–407.
Kanyanta, V., 2009. Towards Early Diagnosis of Atherosclerosis: Wall Shear Prediction. University College Dublin, Ireland Ph.D. thesis.
Kanyanta, V., Ivankovic, A., 2009. Mechanical charaterisation of polyurethane elastomer for biomedical applications, Journal of the Mechanical Behavior of Biomedical Materials, in press, doi:10.1016/j.jmbbm.2009.03.005.
Karac, A., Ivankovic, A., 2003. Modelling the drop impact behaviour of fluid-filled polyethylene containers. In: Fracture of Polymers, Composites and Adhesives II, Vol. 32. ESIS Publication, Elsevier Ltd, pp. 253–264.
Khir, A.W., Swalen, M.J., Feng, P.J., Parker, K.H., 2007. Simultaneous determination of wave speed and arrival time of reflected waves using the pressure–velocity loop. Medical and Biological Engineering and Computing 45, 120110.
Kittisak, K., Ramana, M.P., 2008. Inhalation induced stresses and flow characteristics in human airways through fluid–structure interaction analysis. Modelling and Simulation in Engineering 2008 (Article ID 358748).
Kock, S.A., Nygaard, J.V., Eldrup, N., Fründ, E.T., Klaerke, A., Paaske, W.P., Falk, E., Yong Kim, W., 2008. Mechanical stresses in carotid plaques using MRI-based fluid-structure interaction models. Journal of Biomechanics 41 (8), 1651–1658.
Myers, J.G., Moore, J.A., Ojha, M., Johnson, K.W., Ethier, C.R., 2001. Factors influencing blood flow patterns in the human right coronary artery. Annals of Biomedical Engineering 29 (2), 109–120.
Nobili, M., Morbiducci, U., Ponzini, R., Del Gaudio, C., Balducci, A., Grigioni, M., Maria, M.F., Redaelli, A., 2008. Numerical simulation of the dynamics of a bileaflet prosthetic heart valve using a fluid-structure interaction approach. Journal of Biomechanics 41 (11), 2539–2550.
Pivkin, I., Richardson, P., Laidlaw, D., Karniadakis, G., 2004. Effects of cardiac motion on right coronary artery hemodynamics. Journal of Biomechanics 38 (6), 1283–1290.
Scotti, C.M., Jimenez, J., Muluk, S.C., Finol, E.A., 2008. Wall stress and flow dynamics in abdominal aortic aneurysms: finite element analysis vs. fluid-structure interaction. Computer Methods in Biomechanics and Biomedical Engineering 11 (3), 301–322.
Steinman, D.A., Poepping, T.L., Tambasco, M., Rankin, R.N., Holdsworth, D.W., 2000. Flow patterns at the stenosed carotid bifurcation: effects of concentric versus eccentric stenosis. Annals of Biomedical Engineering 28 (4), 415–423.
Steinman, D.A., Thmas, J.B., Ladak, H.M., Milner, J.S., Rutt, B.K., Spence, J.D., 2002. Reconstruction of carotid bifurcation hemodynamics and wall thickness using computational fluid dynamics and MRI. Magnetic Resonance in Medicine 47 (1), 149–159.
Tijsseling, A.S., Lambert, M.F., Simpson, A.R., Stephens, M.L., Vtkovsk, J.P., Bergant, A., 2006. Wave front dispersion due to fluid-structure interaction in long liquid-filled pipelines. In: Proceedings 23rd IAHR Symposium on Hydraulic Machinery and Systems, Yokohama, Japan, October 17–21, 2006. Engineering in Medicine and Biology Society. Paper 143 IAHR.
Wiggert, D.C., Tijsseling, A.S., 2001. Fluid transients and fluid-structure interaction in flexible liquid-filled piping. Applied Mechanics Reviews 54, 456–481.
Wylie, E.B., Streeter, V.L., 1993. Fluid Transients in Systems. Prentice Hall, Englewood Cliffs, New York 〈www.wikki.co.uk〉 Open source CFD solution for research and industry.
Yang, X.L., Liu, Y., Yang, J.M., 2007. Fluid–structure interaction in a pulmonary arterial bifurcation. Journal of Biomechanics 40 (12), 2694–2699.
Zeng, D., Ding, Z., Friedman, M.H., Ethier, C.R., 2003. Effects of cardiac motion on right coronary artery hemodynamics. Annals of Biomedical Engineering 31, 420–429.